(article starts on next page)

A micromechanically based model for dynamic damage evolution in unidirectional composites

R. Larsson [a,*], V. Singh [b,a], R. Olsson [b,a], E. Marklund [b]

[a] *Division of Material and Computational Mechanics, Department of Industrial and Materials Science Chalmers University of Technology, SE-412 96, Göteborg, Sweden*
[b] *Division of Materials and Production, RISE SICOMP, SE-431 22, Mölndal, Sweden*

ABSTRACT

This article addresses the micromechanically motivated, quasistatic to dynamic, failure response of fibre reinforced unidirectional composites at finite deformation. The model draws from computational homogenization, with a subscale represented by matrix and fibre constituents. Undamaged matrix response assumes isotropic viscoelasticity–viscoplasticity, whereas the fibre is transversely isotropic hyperelastic. Major novelties involve damage degradation of the matrix response, due to shear in compression based on a rate dependent damage evolution model, and the large deformation homogenization approach. The homogenized quasi-brittle damage induced failure is described by elastically stored isochoric energy and plastic work of the undamaged polymer, driving the evolution of damage. The developed model is implemented in ABAQUS/Explicit. Finite element validation is carried out for a set of off-axis experimental compression tests in the literature. Considering the unidirectional carbon–epoxy (IM7/8552) composite at different strain rates, it appears that the homogenized damage degraded response can represent the expected ductile failure of the composite at compressive loading with different off-axes. Favourable comparisons are made for the strain and fibre rotation distribution involving localized shear and fibre kinking.

1. Introduction

Polymer matrix composites are finding increased use in areas such as aerospace, automotive, and civil infrastructure because they can be produced with desirable stiffness and strength-to-weight properties (Zhu et al., 2018). They also provide higher passenger safety in automotive owing to better energy dissipation per unit weight in case of collision (Mamalis et al., 1997). In applications involving crash and impact events, a very important property is how structural composites can sustain impact and other dynamic loads, where quasi-brittle failure due to compressive off-axis loading is very crucial. In this context, carbon fibre epoxy systems are mostly considered but composite systems involving thermoplastics are upcoming for improved environmental sustainability. At dynamic loading, fibre reinforced polymers (FRP) demonstrate quite complex strain rate dependent quasi-brittle behaviour due to viscoelastic–viscoplastic characteristics of the polymer matrix, as reported in reviews by Singh (2018) and Sierakowski (1997). Here, failure mechanisms such as fibre kinking and matrix cracking develop gradually in the laminates, leading to a progressive degradation of the material properties.

A thorough understanding of both the microstructural and consequent macroscopic stress–strain response is thus required to capture the high strain rate behaviour occurring at dynamic load. To start with, experimental evidence of viscoelastic/plastic response of the polymer composites in general is due to e.g. Dasappa et al. (2009), Pupure et al. (2018), Marklund et al. (2008) and, in particular, due to Koerber et al. (2010) for the current investigated IM7/8552 carbon–epoxy material. As to modelling, there are only a few dynamic constitutive models for polymeric composites, which with the consequent FE implementation address the nonlinear strain rate effect coupled to material degradation combined with anisotropy and heterogeneity induced by fibre reinforcement. In Kaliske (2000) a kinematically nonlinear model is presented for unidirectional composites involving rate dependence through viscoelasticity. We mention Gerbaud et al. (2019), Eskandaria et al. (2019), and Koerber et al. (2018), who present a phenomenological invariant based formulations to represent viscoelastic and/or viscoplastic effects in polymer composites without degradation modelling. Camanho et al. (2013) developed a material degradation model including the material heterogeneity based on the smeared crack approach. Melro et al. (2013) developed a constitutive damage model for an epoxy matrix based on micromechanical analysis of polymer composite materials. A continuum damage model for prediction of

---

the onset and evolution of intralaminar failure mechanisms and the collapse of structures manufactured in fibre-reinforced plastic laminates was proposed by Maimí et al. (2007). Tan and Liu (2020) developed a micromechanically motivated constitutive model to capture the matrix shearing and fibre rotation of carbon fibre reinforced polymers (CFRPs) deformation at different strain rates. Here, the carbon fibre composite was homogenized, based on various inelastic slip systems identified from the fibre architecture. Recently, Larsson et al. (2020) proposed a micromechanical model for polymer composites under quasi-static and high strain rates. In this model, fibres were considered to be a transversely isotropic, linear elastic material and the matrix a pressure sensitive isotropic viscoelastic–viscoplastic material. Computational homogenization was used to connect matrix and fibre constituents in order to establish a model at the ply scale. The developed constitutive model computes the nonlinear, strain rate dependent deformation of polymer composites.

In addition to the strain-rate effects, material degradation due to shear induced damage is an important failure mechanism in polymer composites. Accompanied by significant inelastic deformations coupled to degradation due to damage, this failure mechanism is quasi-brittle, in particular for compressive off-axis loading. Continuum damage formulations for composite systems have previously been adopted by e.g. Ladeveze and LeDantec (1992) and Maimí et al. (2007); also including fibre kinking theory, e.g. Gutkin et al. (2016), Costa et al. (2017). To predict fibre kinking of UD composites under quasi-static compressive loading, a model accounting for damage growth was developed by Larsson et al. (2018). For ductile failure, damage enhanced formulations of "Lemaitre" type (Lemaitre, 1992) have been developed based on continuum thermodynamics. The effective (or undamaged) material response is governed by e.g. viscoplastic behaviour for shear degradation, as described in Razanica et al. (2019) and Larsson et al. (2015, 2020). In this context, much attention has been paid to mesh objective damage models involving regularization mechanisms like rate dependence and gradient damage, cf. the early work by Peerlings et al. (1996), contributions to phase field damage modelling e.g. Miehe et al. (2010b,a), Miehe (2011) including the review by Ambati et al. (2015).

In this contribution, the developments in Larsson et al. (2020) and Razanica et al. (2019) are combined to formulate and implement a damage enhanced continuum of Lemaitre type. Our aim is to capture the quasi-brittle failure process of a UD composite at high strain rate and under compressive loading. The effective material response is described by the viscoelastic–viscoplastic constitutive model in Larsson et al. (2020), where the damage/inelasticity coupling is described in terms of a damage driving energy involving elastic and inelastic contributions of the effective material response, cf. Larsson et al. (2015, 2020). In view of the application to crash events of the structural response, the formulation (Larsson et al., 2020) is extended to nonlinear kinematics. The model has been implemented as a VUMAT subroutine in Abaqus/Explicit dynamic events. The proposed model predicts the onset of intralaminar failure mechanisms such as fibre kinking and matrix failure at different strain rates applied to off-axis UD composite specimens under compressive loading.

2. Homogenized response of matrix–fibre composite

2.1. Approach

In this subsection we give the main steps to the homogenized response of the matrix–fibre composite in context of nonlinear kinematics. To this end, consider an RVE $B^0_\square$ of the reference (undeformed) configuration for the UD composite in Fig. 1. The matrix material is in the region $B^{0,\mathrm{m}}_\square$ and the fibre material is in the region $B^{0,\mathrm{f}}_\square$. Consider the RVE subjected to the constant Lagrangian strain $\bar{E}$ in $B^0_\square$ written as

$$\bar{E} = \frac{1}{2}\left(\bar{F}^t \cdot \bar{F} - \mathbf{1}\right) \tag{1}$$

where $\bar{F}$ is the macroscopic deformation gradient.

To describe the microscopic strain field E locally in $B^0_\square$, it is assumed that the strain consists of the constant (average) part $\bar{E}$ and an oscillating sub-scale portion $\tilde{E} = a\hat{E} \in B^0_\square$, where $\hat{E} := \bar{E} : I_{\bar{E}}$. Here, $I_{\bar{E}}$ is a fourth order operator defining the projection of the macroscopic strain onto the sub-scale. Moreover, a is a scalar field in $B^0_\square$ representing the local variation of the projected macroscopic strain $\hat{E}$. The total Lagrange strain is thus

$$E = \bar{E} + \tilde{E} \in B^0_\square \Rightarrow \delta E = \left(I + a\,I_{\bar{E}}\right) : \delta\bar{E} + (\bar{E} : I_{\bar{E}})\delta a \in B^0_\square \tag{2}$$

The Hill–Mandel condition states that the homogenized virtual work at the macroscopic level equals the virtual work done by the microscopic strain and stress fields in the RVE domain. In view of (2), this homogenization principle is formulated as

$$\delta\bar{E} : \bar{S} = \delta\bar{E} : \left\langle\left(I + a\,I_{\bar{E}}\right) : S\right\rangle_{B^0_\square} + \hat{E} : \langle\delta a\,S\rangle_{B^0_\square} \;\forall\delta a \tag{3}$$

where the volume mean of $B^0_\square$ is defined through $V_\square\langle\bullet\rangle_{B^0_\square} = \int_{B^0_\square} \bullet\, dB$.

The Hill–Mandel relation in (3) yields the homogenized macroscopic stress

$$\bar{S} = \left\langle\left(I + a\,I_{\bar{E}}\right) : S\right\rangle_{B^0_\square} \tag{4}$$

corresponding to micromechanical equilibrium represented by the weak form

$$\hat{E} : \langle\delta a\,S[a]\rangle_{B^0_\square} = 0 \;\forall\delta a \tag{5}$$

We also consider the corresponding kinematic compatibility condition formulated as

$$\left\langle\delta S : \left(a\,\bar{E} : I_{\bar{E}}\right)\right\rangle_{B^0_\square} = \delta\bar{S} : \langle a\,\bar{E} : I_{\bar{E}}\rangle_{B^0_\square} = 0 \Leftrightarrow \boxed{\langle a\rangle_{B^0_\square} = 0} \tag{6}$$

whereby (since $\bar{E}$ is constant in the RVE) the local scalar field a has a vanishing mean in the RVE domain.

2.2. Matrix–fibre composite

Following Larsson et al. (2020), a simple but representative homogenized response of the composite is assumed from a *piecewise constant* scalar field a in $B^0_\square$ so that

$$\tilde{E} := a\,\hat{E} \tag{7}$$

where

$$a = \begin{cases} a^{\mathrm{f}} & X \in B^{0,\mathrm{f}}_\square \\ a^{\mathrm{m}} & X \in B^{0,\mathrm{m}}_\square \end{cases} \;,\; S = \begin{cases} S^{\mathrm{f}} & X \in B^{0,\mathrm{f}}_\square \\ S^{\mathrm{m}} & X \in B^{0,\mathrm{m}}_\square \end{cases} \tag{8}$$

The kinematic compatibility condition (6) yields the consequent piece-wise constant a scalar field as

$$\int_{B^0_\square} a\, dB = v^{\mathrm{m}} a^{\mathrm{m}} + v^{\mathrm{f}} a^{\mathrm{f}} = 0 \Rightarrow \boxed{a^{\mathrm{f}} = -\frac{v^{\mathrm{m}}}{v^{\mathrm{f}}} a^{\mathrm{m}}} \tag{9}$$

Here $v^{\mathrm{f}} = V^{\mathrm{f}}_\square/V_\square$ is the volume fraction fibres and $v^{\mathrm{m}} = V^{\mathrm{m}}_\square/V_\square$ is the volume fraction of matrix material. They have the relation $v^{\mathrm{m}} + v^{\mathrm{f}} = 1$.

The projected macroscopic strain $\hat{E}$ is chosen to represent straining solely transverse to the fibre direction. To this end, we make the following assumptions for the stress/strain state of the RVE in Fig. 1:

1. A constant strain is assumed in the fibre direction, i.e. fibres and matrix locally experience uniform and equal strains.
2. A piecewise constant strain is assumed in shearing and transverse to fibres, i.e. fibres and matrix locally experience uniform and equal stresses ("constant stress").

The first assumption is justified by virtue of strain compatibility during extension in the fibre direction, whereas the second assumption is an obvious simplification to allow efficient homogenization. By virtue of equilibrium transverse to fibres, assumption 2 is fully valid for a 2D
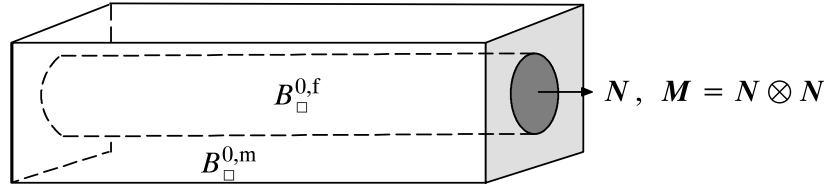
Fig. 1. Representative volume element with volume $V_\square$ with a fibre region $B_\square^{0,f} \in B_\square^0$ (who has the orientation tensor $\boldsymbol{M}$ in material configuration) embedded into the polymer matrix $B_\square^{0,m}$ in $B_\square^0$.

composite with 'fibres' being slabs of uniform thickness. For composites with circular fibres micro-stresses are highly nonuniform during shearing or transverse loading, but stresses in matrix and fibres will be equal in an average sense. In the plastic range the stresses in shear and transverse loading will become increasingly uniform, whereas the strains remain nonuniform.

The transverse strain $\hat{\boldsymbol{E}}$ is thus defined from the projection $\hat{\boldsymbol{I}} = \boldsymbol{I}_{\bar{E}}$ defined as

$$\hat{\boldsymbol{E}} := (\bar{\boldsymbol{E}} \cdot \hat{\boldsymbol{I}})^{\text{sym}} = \hat{\boldsymbol{I}} : \bar{\boldsymbol{E}} \text{ with } \hat{\boldsymbol{I}} := \frac{1}{2}\left(\mathbf{1}\bar{\otimes}\hat{\mathbf{1}} + \hat{\mathbf{1}}\bar{\otimes}\mathbf{1}\right) \qquad (10)$$

where the dyadic product $\bar{\otimes}$ is introduced to denote the representation of a fourth order tensor structure $\boldsymbol{A} = \boldsymbol{a}\bar{\otimes}\boldsymbol{b}$ in terms of the second order tensors $\boldsymbol{a}$ and $\boldsymbol{b}$. This structure is defined by $(\boldsymbol{a}\bar{\otimes}\boldsymbol{b}) : \boldsymbol{c} = \boldsymbol{a} \cdot \boldsymbol{c} \cdot \boldsymbol{b}^t$. Evidently, $\hat{\boldsymbol{E}}$ is now the macroscopic strain projected onto the transverse direction of the fibres, governed the second order isotropy plane identity $\hat{\mathbf{1}}$. This tensor is defined via $\hat{\mathbf{1}} := \mathbf{1} - \boldsymbol{M}$ and $\boldsymbol{M}$ is the fibre orientation tensor in $B_\square^0$, as shown in Fig. 1.

With the assumption about piecewise constant fields, the micromechanical equilibrium problem (5) directly reduces to

$$\delta a^m \, v^m \, \hat{\boldsymbol{E}} : \left(\boldsymbol{S}^m - \boldsymbol{S}^f\right) = 0 \qquad (11)$$

corresponding the desired *scalar fibre transverse stress continuity condition* between the different phases of straight and misaligned fibres of the RVE.

We also find that the homogenized (continuum) stress in (4) is obtained as

$$\bar{\boldsymbol{S}} = \langle (\boldsymbol{I} + a\,\hat{\boldsymbol{I}}) : \boldsymbol{S} \rangle_{B_\square^0} = v^m \, \boldsymbol{S}^m + v^f \, \boldsymbol{S}^f + a^m \, v^m \, \hat{\boldsymbol{I}} : \left(\boldsymbol{S}^m - \boldsymbol{S}^f\right) \qquad (12)$$

representing a non-standard homogenization result for $a^m \neq 0$ due to the presence of the macroscopic transverse strain $\hat{\boldsymbol{E}}$.

2.3. Push-forward to spatial configuration

In order to the express the homogenized response in spatial form let us consider the microscopic Lagrangian strain rate

$$\dot{\boldsymbol{E}} = \left(\boldsymbol{I} + a\,\hat{\boldsymbol{I}}\right) : \dot{\bar{\boldsymbol{E}}} + \hat{\boldsymbol{I}} : \bar{\boldsymbol{E}}\,\dot{a} \qquad (13)$$

and the consequent work rate

$$\boldsymbol{S} : \dot{\boldsymbol{E}} = \left(\boldsymbol{S} + a\,\hat{\boldsymbol{S}}\right) : \dot{\bar{\boldsymbol{E}}} + \hat{\boldsymbol{S}} : \bar{\boldsymbol{E}}\dot{a} \qquad (14)$$

Push forward is then conveniently obtained with respect to the macroscopic deformation gradient as $\dot{\bar{\boldsymbol{E}}} = \bar{\boldsymbol{F}}^t \cdot \bar{\boldsymbol{d}} \cdot \bar{\boldsymbol{F}}$, where $\bar{\boldsymbol{d}}$ is the macroscopic rate of deformation tensor. The relation (14) is now worked out as

$$\boldsymbol{S} : \dot{\boldsymbol{E}} = (\boldsymbol{\tau} + a\,\hat{\boldsymbol{\tau}}) : \bar{\boldsymbol{d}} + \hat{\boldsymbol{\tau}} : \frac{1}{2}\left(\mathbf{1} - \bar{\boldsymbol{b}}^{-1}\right)\dot{a} \qquad (15)$$

where the Kirchhoff stresses are $\boldsymbol{\tau} = \bar{\boldsymbol{F}} \cdot \boldsymbol{S} \cdot \bar{\boldsymbol{F}}^t$, $\hat{\boldsymbol{\tau}} = \bar{\boldsymbol{F}} \cdot \hat{\boldsymbol{S}} \cdot \bar{\boldsymbol{F}}^t$ and $\bar{\boldsymbol{b}} = \bar{\boldsymbol{F}} \cdot \bar{\boldsymbol{F}}^t$ is the Finger tensor. Here, it may be noted that $\hat{\boldsymbol{\tau}} = \boldsymbol{\tau} : \hat{\boldsymbol{i}}$ where $\hat{\boldsymbol{i}}$ is the spatial transverse projection operator

$$\hat{\boldsymbol{i}} = \frac{1}{2}\left(\mathbf{1}\bar{\otimes}\boldsymbol{i} + \boldsymbol{i}\bar{\otimes}\mathbf{1}\right) \text{ with } \boldsymbol{i} = \bar{\boldsymbol{F}}^{-t} \cdot \hat{\mathbf{1}} \cdot \bar{\boldsymbol{F}}^t \qquad (16)$$

In view of the sequel (3)–(6), the homogenization in spatial form thus follows as

$$\bar{\boldsymbol{\tau}} = \langle (\boldsymbol{I} + a\,\hat{\boldsymbol{i}}) : \boldsymbol{\tau} \rangle_{B_\square^0} = v^m \boldsymbol{\tau}^m + v^f \boldsymbol{\tau}^f + a^m v^m \hat{\boldsymbol{i}} : \left(\boldsymbol{\tau}^m - \boldsymbol{\tau}^f\right) \qquad (17)$$

together with

$$\left(\boldsymbol{\tau}^m - \boldsymbol{\tau}^f\right) : \hat{\boldsymbol{e}} = 0 \text{ with } \hat{\boldsymbol{e}} = \hat{\boldsymbol{i}} : \bar{\boldsymbol{e}} \text{ and } \bar{\boldsymbol{e}} = \frac{1}{2}\left(\mathbf{1} - \bar{\boldsymbol{b}}^{-1}\right) \qquad (18)$$

Here, $\hat{\boldsymbol{e}}$ is the projected Eulerian strain tensor $\bar{\boldsymbol{e}}$ onto the transverse fibre direction.

3. Constitutive response of matrix and fibre constituents

This section summarizes key development steps to the homogenized response of the composite constituents in Section 2 in the context of nonlinear kinematics. A recent damage degrading model is applied to quasi brittle failure of the polymer matrix, whereas the fibre response is considered elastic. This development represents an extension of Larsson et al. (2020), where the degraded response draws from a damage enhanced effective matrix material model of Lemaitre type, (Larsson et al., 2018; Razanica et al., 2019).

3.1. Viscoelasticity/viscoplasticity coupled to damage of the matrix

Consider the rheological model in Fig. 2 for the viscoelasticity/viscoplasticity coupling in the polymer matrix. As shown in Fig. 2, the model involves six parameters for the nonlinear viscoelastic–viscoplastic response. The parameters are: the quasi-static and dynamic shear moduli, G_1, G_0 (via G_2), the relaxation times t_{2*} and t_* associated with the viscoelastic and viscoplastic response and σ_t, σ_c defining the quasi-static yield stress of the polymer matrix in tension and compression. It is assumed that the "elastic" shear response of the polymer matrix material is viscoelastic combined with a viscoplastic deformation mechanism. This is described in terms of "static" shear modulus G_1 and the dynamic shear stiffness $G_0 = G_1 + G_2$, representing the elastic response at very high loading rates (when the viscoelastic damper has no time to develop viscous deformation). As to viscoplasticity, the damper starts to develop inelastic deformation as soon as the slider start to open as defined in terms of a over stress function, cf. the developments below. In addition, damage evolution is described in terms of both elastic and inelastic deformations. The stresses for initiation of viscoplastic deformation are given by σ_c in compression and σ_t in tension.

3.1.1. Kinematics

The kinematics of the model is first established. To this end, consider particles with position $\boldsymbol{X}$ in the reference configuration $B_\square^{0,m}$, in motion with the nonlinear deformation $\boldsymbol{\varphi}[\boldsymbol{X}, t]$ from $\boldsymbol{X}$ to positions $\boldsymbol{x} \in B_\square^m$ in the current configuration. The deformation gradient is $\boldsymbol{F} = \partial\boldsymbol{\varphi}/\partial\boldsymbol{X}$ and $J = \det[\boldsymbol{F}]$ is the volumetric deformation measure. Let us also consider the deformation gradient subdivided into (reversible) elastic components $\boldsymbol{F}_{e1}$ and $\boldsymbol{F}_{e2}$ related to the first and second elastic spring in Fig. 2, respectively. The total deformation gradient $\boldsymbol{F}$ is thus formed differently depending on the elastic deformation in the springs
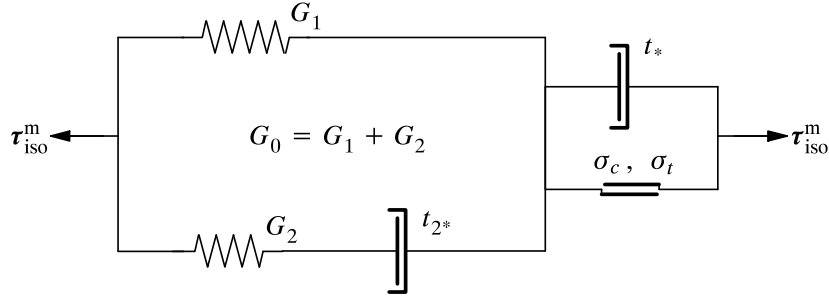
Fig. 2. Rheologcial model for viscoelastic–viscoplastic response of the polymer matrix of the composite. The rheology consists of a viscoelastic 3 parameter response combined with a viscoplastic deformation mechanism.

in terms of the viscous part F_v and the viscoplastic part F_p. The total deformation gradient thus formed multiplicatively as

$$F = F_{e1} \cdot F_p = F_{e2} \cdot F_v \cdot F_p \text{ with } F_{e1} = F_{e2} \cdot F_v \tag{19}$$

Due to the multiplicative split, an additive decomposition of the spatial velocity gradient $l = \dot{F} \cdot F^{-1}$ is obtained in elastic and inelastic portions as

$$l = l_{e1} + l_p = l_{e2} + l_v + l_p \text{ with } l_{e1} = (\dot{F}_{e1} \cdot F_{e1}^{-1})^{\text{sym}} , l_{e2} = (\dot{F}_{e2} \cdot F_{e2}^{-1})^{\text{sym}} \tag{20}$$

where

$$l_p = F_{e1} \cdot L_p \cdot F_{e1}^{-1} \text{ with } L_p = \dot{F}_p \cdot F_p^{-1} \tag{21a}$$

$$l_v = F_{e2} \cdot L_v \cdot F_{e2}^{-1} \text{ with } L_v = \dot{F}_v \cdot F_v^{-1} \tag{21b}$$

where l_v is the viscous velocity gradient (used to represent the viscoelasticity) and the viscoplastic velocity gradient is l_p. Thereby, the relation for the spatial inelastic evolution to the material time derivative is given by

$$\dot{F}_p = F_{e1}^{-1} \cdot l_p \cdot F \text{ and } \dot{F}_v = F_{e2}^{-1} \cdot l_v \cdot F_{e1} \tag{22}$$

We also note that $l_{e2} = l_{e1} - l_v$.

In order to model the matrix material we consider the stored free energy ψ^{m} related to the volume of matrix material in the RVE. This is defined in the contributions

$$\psi^{\text{m}} = f[\alpha] \left(\hat{\psi}_{1,iso}^{\text{m}} + \hat{\psi}_{2,iso}^{\text{m}} \right) + \psi_{vol}^{\text{m}} \tag{23}$$

representing the deviatoric (or shape distortion) energy, the volume change energy and the micro hardening of the matrix material. The intrinsic stored free energies for the matrix material are explicitly defined as

$$\hat{\psi}_{1,iso}^{\text{m}} = \frac{1}{2} G_1 \left(J_{e1}^{-\frac{2}{3}} \mathbf{1} : b_{e1} - 3 \right),$$

$$\hat{\psi}_{2,iso}^{\text{m}} = \frac{1}{2} G_2 \left(J_{e2}^{-\frac{2}{3}} \mathbf{1} : b_{e2} - 3 \right), \psi_{vol}^{\text{m}} = \frac{1}{2} K \log^2[J] \tag{24}$$

where G_1 and G_2 are shear moduli of the viscous shear response, whereas K is the bulk modulus of the matrix material. Moreover, we have generically the elastic spatial deformation tensor $b_e = F_e \cdot F_e^t$ and the volumetric deformation is $J = \det F$. Note that the "shear" response is taken in terms of the isochoric (volume preserving) deformation. The damage variable $0 \leq \alpha \leq 1$ is assumed to degrade shear response of the polymer matrix via the degradation function $f[\alpha]$. Here it is noted that the damage field $\alpha[X] \in B_0$, where B_0 is the region of the solid as discussed in Section 4. Hence, it is assumed that the damage degradation function degrades only the matrix so that $f[0] = 1$ for the virgin polymer and $f[1] = r \approx 0$ for the fully damaged polymer with

$$f[\alpha] = (1 - \alpha)^2 + r \tag{25}$$

whereby $f'[\alpha] < 0$ for $0 \leq \alpha \leq 1$. Here, we remark that compressive fibre fracture in the composite typically occurs at a late stage in the failure scenario, controlled by matrix degradation. Thus, compression along the fibres causes severe softening due to localized fibre rotation ("kinking") enforced by the micro-mechanical equilibrium (11) combined with yielding and damage in the matrix.

From the basic postulate that the mechanical dissipation rate $\mathcal{D}^{\text{m}} \geq 0$ we find that

$$\mathcal{D}^{\text{m}} := \tau^{\text{m}} : d - \dot{\psi}^{\text{m}} =$$

$$\tau^{\text{m}} : d - 2f[\alpha] \left(b_{e1} \cdot \frac{\partial \hat{\psi}_{1,iso}^{\text{m}}}{\partial b_{e1}} + b_{e2} \cdot \frac{\partial \hat{\psi}_{2,iso}^{\text{m}}}{\partial b_{e2}} \right) : d_{e1} +$$

$$f[\alpha] 2 b_{e2} \cdot \frac{\partial \hat{\psi}_{2,iso}^{\text{m}}}{\partial b_{e2}} : d_v - \frac{\partial \psi_{vol}^{\text{m}}}{\partial J} \dot{J} - f'[\alpha] \left(\hat{\psi}_{1,iso}^{\text{m}} + \hat{\psi}_{2,iso}^{\text{m}} \right) \dot{\alpha} =$$

$$f[\alpha] \hat{w}^p + \mathcal{A}\dot{\alpha} \geq 0 \tag{26}$$

where e.g. $d = l^{\text{sym}}$ is the rate of deformation tensor. Here

$$\hat{w}^p := \hat{\tau}_{iso}^{\text{m}} : d_p + \hat{\tau}_{2,iso}^{\text{m}} : d_v \text{ and } \mathcal{A} = -f'[\alpha] \left(\hat{\psi}_{1,iso}^{\text{m}} + \hat{\psi}_{2,iso}^{\text{m}} \right) \tag{27}$$

where $\hat{w}^p$ is the plastic work rate and $\mathcal{A}$ is the elastic damage driving energy.

From (26) with zero elastic dissipation rate, we obtain the constitutive state equations for the total Kirchhoff stress of the matrix as

$$\tau^{\text{m}} = f[\alpha]\hat{\tau}_{iso}^{\text{m}} + \tau_m^{\text{m}}\mathbf{1} \text{ with } \hat{\tau}_{iso}^{\text{m}} = \hat{\tau}_{1,iso}^{\text{m}} + \hat{\tau}_{2,iso}^{\text{m}} \tag{28}$$

where

$$\hat{\tau}_{1,iso}^{\text{m}} = 2b_{e1} \cdot \frac{\partial \hat{\psi}_{1,iso}^{\text{m}}}{\partial b_{e1}} = G_1 J_{e1}^{-\frac{2}{3}} \left(b_{e1} \right)_d \tag{29a}$$

$$\hat{\tau}_{2,iso}^{\text{m}} = 2b_{e2} \cdot \frac{\partial \hat{\psi}_{2,iso}^{\text{m}}}{\partial b_{e2}} = G_2 J_{e2}^{-\frac{2}{3}} \left(b_{e2} \right)_d \tag{29b}$$

$$\tau_m^{\text{m}} = J \frac{\partial \psi_{vol}^{\text{m}}}{\partial J} = K \log[J] \tag{29c}$$

3.1.2. Evolution rules

As the main prototype, we consider with respect to the matrix shear behaviour viscoplastic/viscoelastic evolution rules defined as

$$d_p = \lambda \frac{\partial \phi^*}{\partial \hat{\tau}_{iso}^{\text{m}}} = \lambda f \text{ with } f = \frac{3}{2} \frac{\hat{\tau}_{iso}^{\text{m}}}{\hat{\tau}_e^{\text{m}}} \tag{30a}$$

$$d_v = \frac{1}{2G_2 t_{2*}} \hat{\tau}_{2,iso}^{\text{m}} \tag{30b}$$

where the yield and plastic functions ϕ and ϕ^* are defined as

$$\phi = \hat{\tau}_e^{\text{m}} - \left(\sigma_y + \gamma p \right) , \phi^* = \hat{\tau}_e^{\text{m}} - \sigma_y \text{ with } \hat{\tau}_e^{\text{m}} = \sqrt{\frac{3}{2}} |\hat{\tau}_{iso}^{\text{m}}| \text{ and } p = -\tau_m^{\text{m}} \tag{31}$$

Here, $\hat{\tau}_e^{\text{m}}$ is the effective von Mises stress, γ is the friction parameter in the yield function, t_{2*} is the relaxation time parameter of the elastic

viscous damper and λ is the viscoplastic multiplier obeys the Bingham model

$$\lambda = \frac{1}{t_*}\eta[\phi] \geq 0 \text{ with } \eta[\phi] := \frac{\langle \hat{\tau}_e^{\mathrm{m}} - (c_y + \gamma p)\rangle}{3G_0} \tag{32}$$

where t_* is the viscoplastic relaxation time and η is the Bingham overstress function.

3.1.3. Damage driving energy

For ductile failure processes the damage driving energy is shown to consist of elastically stored free energy and inelastic contributions of the effective (undamaged) material (Razanica et al., 2019). In the present paper we follow the same idea to describe quasi-brittle failure for the polymer matrix, where both elastic and inelastic, in particular viscoplastic, mechanisms are contributing. The damage/elasticity/inelasticity coupling is obtained by reformulating the dissipation rate $\mathcal{D}^{\mathrm{m}}$ in (26) in the total dissipation. In view of (26), this is defined in terms for the total (integrated) effective plastic work $\hat{W}^p = \int_0^t \hat{w}^p dt$ as

$$\mathcal{D}_{\mathrm{T}}^{\mathrm{m}} := \int_0^t \mathcal{D}^{\mathrm{m}} dt = f[\alpha]\hat{W}^p + \int_0^\alpha \mathcal{A}_{\mathrm{T}} d\alpha \geq 0 \tag{33}$$

where $\mathcal{A}_{\mathrm{T}}$ is the damage driving energy

$$\mathcal{A}_{\mathrm{T}} = \mathcal{A} + \mathcal{B} \text{ with } \mathcal{A} = -f[\alpha](\hat{\psi}_{1,\mathrm{iso}}^{\mathrm{m}} + \hat{\psi}_{2,\mathrm{iso}}^{\mathrm{m}}) \text{ and } \mathcal{B} = -f[\alpha]\hat{W}^p \tag{34}$$

Here, $\mathcal{A}_{\mathrm{T}}$ consists of elastic and inelastic contributions $\mathcal{A}$ and $\mathcal{B}$, respectively. The elastic stored free energy contribution $\mathcal{A}$ initiates instantaneously as shown by Eq. (34), whereas the inelastic contribution $\mathcal{B}$ initiates as viscoplasticity commences. It is thus assumed that the elastic stored energy due the quasi-static and dynamic shear mechanisms and the corresponding inelastic work of the effective material are to be dissipated during the damage evolution process.

3.2. Transverse hyperelastic fibre response

A transversely isotropic hyperelastic fibre response is assumed as a direct extension of the geometrically linear elastic material model in Larsson et al. (2018) to the geometrically nonlinear regime. Hence, the total elastic response is obtained from the stored free energy ψ^{f} in the four strain energy portions

$$\psi^{\mathrm{f}} = \psi_d^{\mathrm{f}} + \psi_{vol}^{\mathrm{f}} + \psi_s^{\mathrm{f}} + \psi_a^{\mathrm{f}} \tag{35}$$

where the deviatoric (or shape distortion) energy and the volume change energy are represented by the ψ_d^{f} and ψ_{vol}^{f}, respectively, for the fibre material. These stored energies are formulated in terms of invariants of the Lagrange strain $\boldsymbol{E}$ and its deviatoric portion $\boldsymbol{E}_{\mathrm{d}}$ defined as

$$\psi_d^{\mathrm{f}} = \frac{1}{2}2G_d^{\mathrm{f}}\boldsymbol{E}_{\mathrm{d}} : \boldsymbol{E}_{\mathrm{d}} , \ \psi_{vol}^{\mathrm{f}} = \frac{1}{2}K^{\mathrm{f}}(\mathbf{1} : \boldsymbol{E})^2 \tag{36}$$

where the shear modulus G_d^{f} and the bulk modulus K^{f} of the fibre.

The anisotropic part of the stored free fibre energy consists of the longitudinal fibre shear ψ_s^{f} and the axial fibre action ψ_a^{f} written as

$$\psi_s^{\mathrm{f}} = \frac{1}{2}G_s^{\mathrm{f}}\gamma^2 , \ \psi_a^{\mathrm{f}} = \frac{1}{2}E^{\mathrm{f}}\left(1 + v^{\mathrm{f}}\right)E^2 \text{ with } E = \frac{\left(1 - 2v^{\mathrm{f}}\right)E_a + v^{\mathrm{f}}E_{vol}}{\left(1 - 2v^{\mathrm{f}}\right)\left(1 + v^{\mathrm{f}}\right)} \tag{37}$$

where γ is the longitudinal fibre shear, and E is the uniaxial fibre strain, related to the (kinematic) axial fibre strain $E_a = \boldsymbol{M} : \boldsymbol{E}$ via the uniaxial fibre response and the volumetric strain $E_{vol} = \mathbf{1} : \boldsymbol{E}$, cf. Larsson et al. (2018). Here, $\boldsymbol{M} = \boldsymbol{N} \otimes \boldsymbol{N}$ is the structural tensor of the fibre orientation. It appears that the fibre shear γ is related to the fibre orientation via $\gamma^2 = 2\boldsymbol{E}_{\mathrm{s}} : \boldsymbol{E}_{\mathrm{s}}$, where $\boldsymbol{E}_{\mathrm{s}}$ is the fibre shear strain tensor

$$\boldsymbol{E}_{\mathrm{s}} = \frac{1}{2}\left(\boldsymbol{E} \cdot \boldsymbol{M} + \boldsymbol{M} \cdot \boldsymbol{E}\right) - \left(\boldsymbol{M} : \boldsymbol{E}\right)\boldsymbol{M} \tag{38}$$

Moreover, in (37) G_s^{f} is the longitudinal fibre shear modulus, E^{f} is the longitudinal fibre modulus of elasticity, and v^{f} is Poisson's ratio of the multiaxial response of the fibre in its longitudinal direction, (Larsson et al., 2018).

Hyperelastic response of fibre material means that the 2nd Piola Kirchhoff stress is

$$\boldsymbol{S} = \frac{\partial\psi^{\mathrm{f}}}{\partial\boldsymbol{E}} = \boldsymbol{S}_d^{\mathrm{f}} + S_m^{\mathrm{f}}\mathbf{1} + \boldsymbol{S}_s^{\mathrm{f}} + S_a^{\mathrm{f}}\boldsymbol{M} \tag{39}$$

where the individual stress contributions are

$$\boldsymbol{S}_d^{\mathrm{f}} = \frac{\partial\psi_d^{\mathrm{f}}}{\partial\boldsymbol{E}_d} = 2G_d^{\mathrm{f}}\boldsymbol{E}_d \tag{40a}$$

$$\boldsymbol{S}_s^{\mathrm{f}} = \frac{\partial\psi_s^{\mathrm{f}}}{\partial\boldsymbol{\epsilon}_s} = 2G_s^{\mathrm{f}}\boldsymbol{E}_s \tag{40b}$$

$$S_m^{\mathrm{f}} = K^{\mathrm{f}}E_{vol} + \frac{v^{\mathrm{f}}}{1 - 2v^{\mathrm{f}}}E^{\mathrm{f}}E_a \tag{40c}$$

$$S_a^{\mathrm{f}} = \frac{1}{1 + v^{\mathrm{f}}}\frac{\partial\psi_a^{\mathrm{f}}}{\partial\epsilon} = E^{\mathrm{f}}E_a \tag{40d}$$

Push forward to spatial coordinates is known in terms of the transformation involved in (15), which yields the Kirchhoff stress as $\boldsymbol{\tau}^{\mathrm{f}} = \bar{\boldsymbol{F}} \cdot \boldsymbol{S}^{\mathrm{f}} \cdot \bar{\boldsymbol{F}}^t$. This gives the total Kirchhoff stress as $\boldsymbol{\tau}^{\mathrm{f}} = \boldsymbol{\tau}_d^{\mathrm{f}} + \boldsymbol{\tau}_m^{\mathrm{f}} + \boldsymbol{\tau}_s^{\mathrm{f}} + \boldsymbol{\tau}_a^{\mathrm{f}}$ where

$$\boldsymbol{\tau}_d^{\mathrm{f}} = \bar{\boldsymbol{F}} \cdot \boldsymbol{S}_d^{\mathrm{f}} \cdot \bar{\boldsymbol{F}}^t \tag{41a}$$

$$\boldsymbol{\tau}_m^{\mathrm{f}} = S_m^{\mathrm{f}}\bar{\boldsymbol{b}} \tag{41b}$$

$$\boldsymbol{\tau}_s^{\mathrm{f}} = \bar{\boldsymbol{F}} \cdot \boldsymbol{S}_s^{\mathrm{f}} \cdot \bar{\boldsymbol{F}}^t \tag{41c}$$

$$\boldsymbol{\tau}_a^{\mathrm{f}} = S_a^{\mathrm{f}}\bar{\boldsymbol{F}} \cdot \boldsymbol{M} \cdot \bar{\boldsymbol{F}}^t = S_a^{\mathrm{f}}\boldsymbol{m} \tag{41d}$$

Here, $\boldsymbol{m} = \boldsymbol{n} \otimes \boldsymbol{n}$ is the spatial fibre structural tensor where the fibre orientation transforms with the deformation gradient as $\boldsymbol{n} = \bar{\boldsymbol{F}} \cdot \boldsymbol{N}$, cf. Fig. 3.

4. Rate dependent damage evolution

This section describes damage degradation of the material to predict the onset and evolution of global failure of the fibre reinforced solid. Thereby, the damage field $\alpha[\boldsymbol{X}] \in B_0$ acts on the macroscale and degrades the polymer locally in $B_{\square}^{0,\mathrm{m}}$ of the microstructure at each material point $\boldsymbol{X}$ of the solid, as discussed in Section 3.1. The damage field is generally both diffusive and localized in character, where the localization of the damage in a localized band of finite width is highlighted in Fig. 4. A diffuse fracture area is obtained by considering the fracture surface smeared out across the internal length l_c. The smearing is assumed to depend on the damage variable itself and its rate $\dot{\alpha}$ (for damage nucleation) through the global fracture area functional $\mathcal{A}_1$ defined as

$$\mathcal{A}_1 = \int_{B_0} \gamma dB \text{ with } \gamma = \int_0^\alpha \left(\frac{\alpha}{l_c} + \frac{\dot{\alpha}}{v^*}\right)d\alpha \tag{42}$$

where γ is the fracture area density per unit internal length of the fracture surface. Evidently, the fracture area density takes on values based on damage state α and the rate of damage $\dot{\alpha}$. The internal length parameter l_c describes the diffusive character of the fracture area, and v^* is the fracture area progression speed parameter, controlling the damage evolution rate $\dot{\alpha}$. The internal length thus controls the width of the damage localization zone, interpreted as the width of the matrix shear failure zone. In the damage zone the rate of change of the fracture area is

$$\dot{\gamma} = \frac{1}{l_c}\alpha\dot{\alpha} + \frac{1}{v^*}\dot{\alpha}^2 \geq 0 \tag{43}$$

To complete the damage evolution model, we establish the balance between *produced* dissipation rate due to fracture surface area production $\mathcal{G}_c\dot{\gamma}$ (where $\mathcal{G}_c$ is the fracture energy) and *supplied* continuum
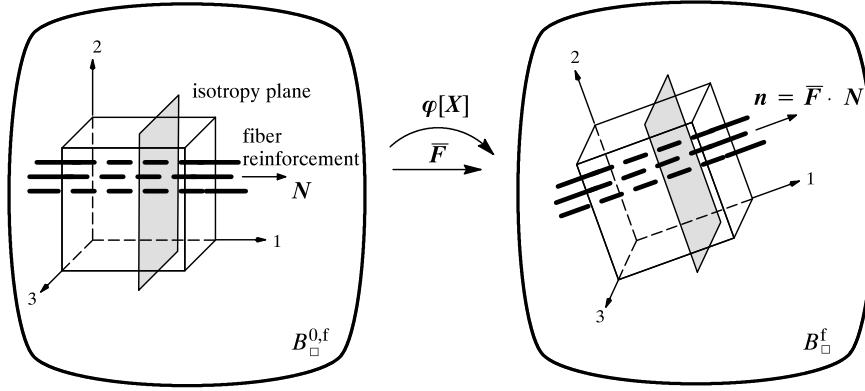
Fig. 3. Fibres in material and spatial configurations, with fibre orientation $N \in B_\square^{0,f}$ and induced spatial orientation $n \in B_\square^f$.
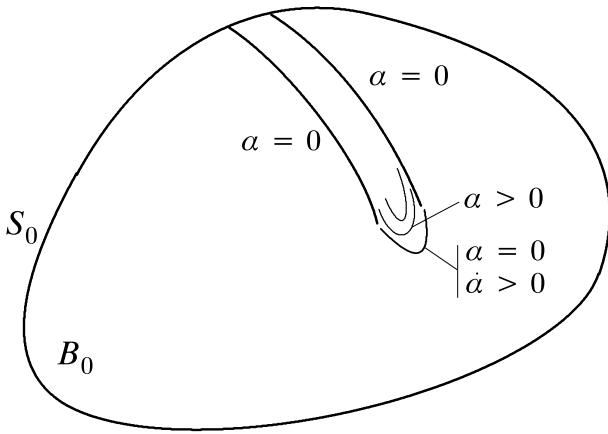

Fig. 4. A damage degrading solid in reference configuration B_0 with a diffusive localized distribution of the damage field in terms of isolevels for α in the progression zone. As indicated, damage progression $\dot{\alpha} > 0$ occurs at the tip of the localization zone.

damage dissipation rate $\mathcal{A}_T \dot{\alpha}$ due to damage driving energy. This balance relationship is thus formulated as

$$\mathcal{G}_c \dot{\gamma} = \mathcal{A}_T \dot{\alpha} \Rightarrow \frac{1}{l_c} \frac{\mathcal{G}_c}{v^*} \left(v^* \alpha + l_c \dot{\alpha} \right) \dot{\alpha} = \mathcal{A}_T \dot{\alpha} \tag{44}$$

where $\mathcal{A}_T$ is the total damage driving energy from (34). To ensure the key condition that $\dot{\alpha} \geq 0$, a dynamic damage loading function is introduced defined as

$$\phi_\alpha = \mathcal{A}_T - \frac{\mathcal{G}_c}{l_c v^*} \left(v^* \alpha + l_c \dot{\alpha} \right) \tag{45}$$

subjected to the damage loading conditions

$$\phi_\alpha \leq 0, \ \dot{\alpha} \geq 0, \ \phi_\alpha \dot{\alpha} = 0 \tag{46}$$

Respecting these damage loading conditions, we immediately obtain the damage evolution as the Bingham type damage evolution law

$$l_c \dot{\alpha} = v^* \langle \alpha^s[\alpha] - \alpha \rangle \text{ with } \alpha^s = \frac{\mathcal{A}_T[\alpha] l_c}{\mathcal{G}_c} \tag{47}$$

where α^s represents the static damage (corresponding to $v^* \to \infty$) due to elastic and inelastic deformation. In the modelling of the fracture surface propagation, the progression speed parameter v^* controls the damage progression $\dot{\alpha}$. We choose v^* large enough to represent the proper static fracture area progression and small enough to achieve stable numerical solution and mesh objectivity for a reasonable time step size. However, in practice it suffices to choose v^* significantly larger than the applied displacement rate, cf. the discussion in Section 5.2.

5. Model validation for a UD composite in compression

The model is validated by comparing the finite element predictions with published experimentally measured stress–strain responses of a UD polymer composite subjected to quasi-static and dynamic off-axis compressive loading.

5.1. Numerical implementation

The proposed rate dependent damage model is implemented in the finite element code Abaqus/Explicit to simulate off-axis compression tests performed by Koerber et al. (2010) on the UD composite through the user defined material subroutine VUMAT. The type of element used is the 8-node brick, C3D8R, with reduced integration and enhanced hourglass control. The mesh was based on equally sized hexahedral solid elements with a uniform edge length of 0.4 mm. Moreover, for computational efficiency hypo-inelasticity was considered in the implementation of the polymer matrix, although the viscous model response is formally phrased in the hyper-inelastic framework in Section 3.1. This assumption works well for "small" elastic deformations as discussed in Ljustina et al. (2012). Hypoelastic–inelastic response is then postulated in rate form of the effective Kirchhoff stresses as

$$\overset{\square}{\hat{\tau}}{}^m := E_e : \left(d - d_p \right) - 2G_2 d_v \text{ with } E_e = 2G_0 I_d^{\text{sym}} + K \mathbf{1} \otimes \mathbf{1} \tag{48a}$$

$$\overset{\square}{\hat{\tau}}{}^m_{2,iso} := 2G_2 I_d^{\text{sym}} : \left(d - d_p - d_v \right) \tag{48b}$$

where e.g. $\overset{\square}{\hat{\tau}}{}^m$ is the Oldroyd rate of the effective stress and I_d^{sym} is the symmetric fourth order deviatoric projection tensor. The backward Euler method is then used to integrate the viscoelastic–viscoplastic response, whereby the Cauchy stress update is conveniently obtained from the radial return mapping algorithm developed in Larsson et al. (2020). A Newton–Raphson procedure is used to solve for the local strain fluctuation variable $a := a^m$ by considering the micromechanical equilibrium problem (11). The main steps to obtain the homogenized stress at the integration point level are described in box:

Start Given the macroscopic displacement and velocity fields $\bar{u}[X]$ and $\bar{v}[X]$, the displacement and velocity gradients are $\{\bar{H} = \bar{u} \otimes \nabla_X, \dot{\bar{H}} = \bar{v} \otimes \nabla_X\}$. The corresponding deformation gradients and Jacobian are $\{\bar{F} = 1 + \bar{H}, \dot{\bar{F}} = \dot{\bar{H}}\}$ and $J = \det[\bar{F}]$. From this, the kinematic Lagrange strain and rate deformation tensor are established as

$$\bar{E} = \frac{1}{2}(\bar{F}^t \cdot \bar{F} - 1) \ , \ \bar{d} = (\bar{v} \otimes \nabla)^{\text{sym}} = (\dot{\bar{F}} \cdot \bar{F}^{-1})^{\text{sym}}$$

The matrix and fibre strain enhancements are

$$\hat{E}^m := \hat{E} = \left(\bar{E} \cdot \hat{1}\right)^{\text{sym}}, \hat{E}^f = -\frac{1 - v^f}{v^f}\hat{E}$$

For all Newton iterations

Matrix : the local Lagrange strain is $E = \bar{E} + a\,\hat{E}$. Its material time derivative yields the local rate of deformation as

$$\dot{E} = \bar{F}^t \cdot d \cdot \bar{F} \rightsquigarrow d = \bar{d} + a\left(\bar{d} \cdot i\right)^{\text{sym}} + (\bar{F}^{-t} \cdot \hat{E} \cdot \bar{F}^{-1})\,\dot{a}$$

Given the local rate of deformation d, time step and internal variables, compute/integrate the Kirchhoff stress τ^m from the flow rules in subsection 3.1.2, the damage evolution (47) and (48). Pullback transformation yields the 2nd Piola–Kirchhoff stress from $S^m = \bar{F}^{-1} \cdot \tau^m \cdot \bar{F}^{-t}$.

Fibre : define the local Lagrange strain and compute the 2nd Piola–Kirchhoff stress from subsection 3.2 as

$$E = \bar{E} - a\frac{1 - v^f}{v^f}\hat{E} \rightsquigarrow S^f = S^f[E]$$

Local stress equilibrium : establish $g[a] = (S^m - S^f) : \hat{E} \simeq 0$ and check convergence, $g < \epsilon_{\text{tol}}$; if needed, update iterative improvement

$$a = a - \frac{g}{g'[a]}$$

End

Homogenized stress : Push forward transformation yields

$$\bar{\tau} = \bar{F} \cdot (v^m S^m + v^f S^f + a\,v^m \hat{1} : (S^m - S^f)) \cdot \bar{F}^t$$

5.2. Material selection and properties

The developed model is tested on different numerical simulations for the chosen geometry and material in order to demonstrate capabilities of the proposed damage model. The experimental data used was obtained by Koerber et al. (2010) to study the influence of strain rates on the behaviour of the UD carbon/epoxy off-axis specimen for compression loading. The material consists of an IM7/8552 carbon fibre reinforced epoxy system. The off-axis test specimens consist of 32 plies and have the nominal dimension of $20 \times 10 \times 4$ mm^3. To assess the model behaviour, a compression test under quasi-static and dynamic loading is used. The test specimen with the off-axis angle θ is shown in Fig. 5. The fibre orientation vector is thus $N = \{\cos\theta, \sin\theta, 0\}$. The compressive tests are carried out by applying the prescribed velocity v on the right boundary, corresponding to the quasi-static and high strain rates in Table 1. The plate is free to move in the horizontal direction at the left surface except for the fully constrained midpoint as shown in Fig. 5. Horizontal motion is allowed for all nodes on the right surface. Material parameters of the constituents involved in the micromechanical model are presented in Table 2 and 3. The elastic fibre properties used in the simulations are shown in Table 2. The longitudinal modulus is according to the manufacturer's data (Hexcel Corporation. Stamford, 2020b), and the rest of the fibre properties are estimated based on typical values seen for HS and IM carbon fibres. In addition the fibre volume fraction is $v^f = 57\%$, cf. also Table 3. The
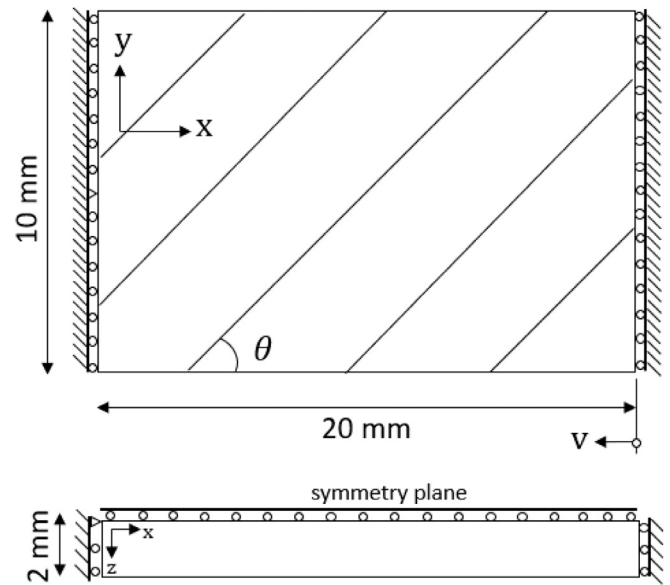

Fig. 5. Specimen geometry for IM7-8552 unidirectional composite laminates of different off-axis angle subjected to compressive loading through the prescribed horizontal velocity v at the right edge.

adopted properties for elastic isotropy of the epoxy 8552 resin (shown in Table 3) were stated in Hexcel Corporation. Stamford (2020a).

5.3. Model parameters and calibration

In this section, the main steps of the model parameter calibration are summarized. The identified model parameters are shown in Table 4. As to the viscoelastic and viscoplastic model parameters, the systematic calibration of the simulated and experimental uniaxial compressive tests has been explained in Larsson et al. (2020). In addition to the six parameters in Section 3.1, three more parameters are needed to model damage and damage evolution to describe the intralaminar failure process of the polymer. These parameters are: the internal length, l_c, the fracture area progression velocity v^* and the fracture energy for the polymer matrix G_c. Therefore, in total nine parameters are needed to capture the nonlinear response of the UD composite in compression under quasi-static and dynamic loading cases.

Some parameters are known from the literature and the estimates (Larsson et al., 2020) are given in Table 3 and the values of G_1, σ_t and σ_c in Table 4. The estimated value of G_c for 8552 epoxy is 1 N/mm, close to 0.68 N/mm stated by the manufacturer. The damage parameter l_c is estimated based on the order of the distance between the fibres in UD composites, i.e. ca. 0.005 mm. Furthermore v^* should be higher than the applied loading rate i.e. $v^* > v$ to properly capture the damage localization in finite element simulation (Razanica et al., 2019). From a set trials with different v^*-values, Table 1 was arrived at without compromising the overall behaviour of the specimen while at the same time preserving stable responses. For the calibration, a least square method is used to find out the best possible fit for the 45° off-axis test specimen of IM7/8552 in quasi-static and dynamic compression. The loading rates considered are: 4×10^{-4}/s in the quasi-static case and 321/s in the dynamic case. The calibration is carried out for a uniaxial test at the *material point level*, as in Larsson et al. (2020) using a MATLAB/FORTRAN implementation. The calibrated response for the 45° off-axis case is shown in Fig. 6, corresponding to the (calibrated) parameters in Table 4. Experiments and model responses in Fig. 6 are shown by dashed and solid lines, whereas quasi-static and dynamic responses are the blue and red coloured solid curves. Damage growth predicted by the model is shown by "semi-solid" (dash–dotted) lines.

Table 1

Considered applied loading rates and consequent (homogeneous) compressive strain rates for the fibre off-axis specimens. The chosen loading is in-line with the experimental strain rates in (Koerber et al., 2018, 2010).

Fibre angle θ	Strain rates in compression [/s]		Loading rate v [mm/s]		Estimated
	Quasi-static	Dynamic	Quasi-static	Dynamic	v^* [mm/s]
15°	4×10^{-4}	122	8×10^{-3}	2440	2500
45°	4×10^{-4}	321	8×10^{-3}	6420	6500
90°	4×10^{-4}	276	8×10^{-3}	5520	5700

Table 2

Material parameters for the carbon fibre.

E_L^f GPa	E_T^f GPa	G_{LT}^f GPa	G_{TT}^f GPa	K_{vol}^f GPa	ν_{LT}^f –	ν_{TT}^f –	v^f %
276	27	30	9.0	24.6	0.25	0.5	57

Table 3

Material parameters for the epoxy at quasi-static loading.

E^m GPa	ν^m –	$G_1 = G^m$ GPa	K^m GPa
4.67	0.37	1.70	5.98
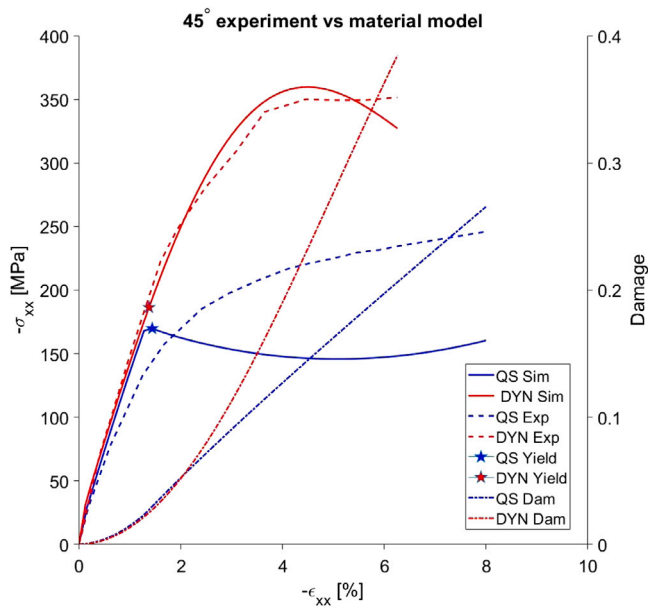
Fig. 6. Uniaxial compressive stress–strain response at the material point level after calibration of the material parameters based on Koerber et al. (2010). The onset of viscoplastic response is indicated by star markers in quasi-static and dynamic loading. (For interpretation of the references to colour in this figure legend, the reader is referred to the web version of this article.)

5.4. Validation

This subsection focuses on the validation of the developed viscoelastic–viscoplastic constitutive model coupled to continuum damage to simulate intralaminar failure of a UD ply. The model predictions are compared with the experimental response of a IM7/8552 carbon–epoxy off-axis composite specimen in compression at different strain rates (Koerber et al., 2010). The model parameters and test setup are shown in Table 3 and Fig. 5. The simulations apply to compressive tests of UD plies with the off-axis angles: 15°, 45° and 90°. For the 90° transverse loading case the total thickness (4 mm) of the specimen was modelled, i.e. the mid-plane symmetry in Fig. 5 was disregarded as shown in Fig. 9(g). It should be noted that fibres rotate anticlockwise, affine with the macroscopic deformation from (41d) and Fig. 3. The

fibre rotation angle β is computed from $\cos \beta = N \cdot n / |n|$. Fig. 7 shows a comparison between the experimental stress–strain response and the corresponding predicted response for the 15° compression test. The quasi-static and dynamic strain rates are shown in Table 1. In order to represent the reported strain measure of the experiment, the stress–strain curves are based on the average strain in a central 3×3 mm region for the quasi-static case and a 6×6 mm region for the dynamic case. This procedure is also used for the rest of the studied off-axis loading cases. The onset of softening along the stress–strain curves of FE simulation is indicated by star markers in Fig. 7(a). The experiments for the 15° compression tests initially show a softer response followed by a higher stress than the model response, which was also observed at the corresponding validation in Larsson et al. (2020). Also note that unloading, due to strain localization emanating from the edges of the specimen, cf. Fig. 7(e), occurs in the centre for dynamic loading, corresponding to the snap-back behaviour in Fig. 7(a). Localized shear bands were observed in the 15° off-axis compression tests at quasi-static and dynamic strain rate. This is a typical longitudinal compressive failure response of unidirectional CFRPs, initiated by the rotation and buckling of misaligned fibres. The predicted and experimentally observed fibre rotation under quasi-static loading are shown in Figs. 7(b)–7(c). For the dynamic loading case in Figs. 7(d)–7(e) the longitudinal strains are considered. There is a good agreement between the experiment and the FE-model for both the kink band formation and magnitudes of the fibre rotations/strains. Fig. 8 shows the experimental behaviour for the 45° off-axis test as compared to the FE simulation using the calibrated parameters from Section 5.3. It is observed that the back calculated (quasi-static and dynamic) stress–strain responses of the specimen based on the FE-simulation agree well with the experimental recording in Fig. 8(a). On the other hand, the material parameters were calibrated at the material point level for this off-axis loading. As to the failure modes, repeated shear bands ca 45° from the loading direction are observed, for both the quasi-static and the dynamic loading cases in Figs. 8(b)–8(e). Since fibres offer little resistance to the applied loading in this case, the failure modes are dominated by pure shear failure of the matrix. There is good qualitative correlation between experimental and simulation results in Fig. 8. For the 90° off-axis test (corresponding to transverse compression) in Fig. 9, the FE-based stress strain response agrees well for the dynamic loading, whereas a too stiff response is obtained for the quasi-static case, cf. Fig. 9(a). In this, case no unloading occurs in the dynamic loading. Diffuse transverse in-plane behaviour is observed for both strain rates, cf. Figs. 9(b)–9(e), whereas 45° out-of-plane shear bands were observed in the x–z plane, cf. Figs. 9(f)–9(g). Under quasi-static loading the fracture is relatively localized, while there are much more cracks in the samples subjected to dynamic loading as shown in Fig. 9.

6. Conclusions

In the present paper we have proposed a rate dependent continuum damage model coupled to a viscoelastic–viscoplastic matrix model. This development is an extension of our previous material model (Larsson et al., 2020) based on micromechanics to include quasi-brittle failure of the UD-composite through continuum damage at finite deformation. To capture the failure mechanisms of unidirectional composites under finite deformation and at different strain rates, the viscoelastic–viscoplastic matrix is degraded based on a rate dependent damage

Table 4

Model parameters for neat epoxy matrix material. The damage progression velocity parameter v^* is not fixed in all simulations as indicated by the • marker.

Calibrated			Estimated				
G_2 Pa	t_{2*} s	t_* s	σ_t MPa	σ_c MPa	$\mathcal{G}_c$ N/mm	l_c mm	v^* mm/s
5.07	8.9×10^{-7}	2.6×10^{-4}	121	180	1	0.005	6500•
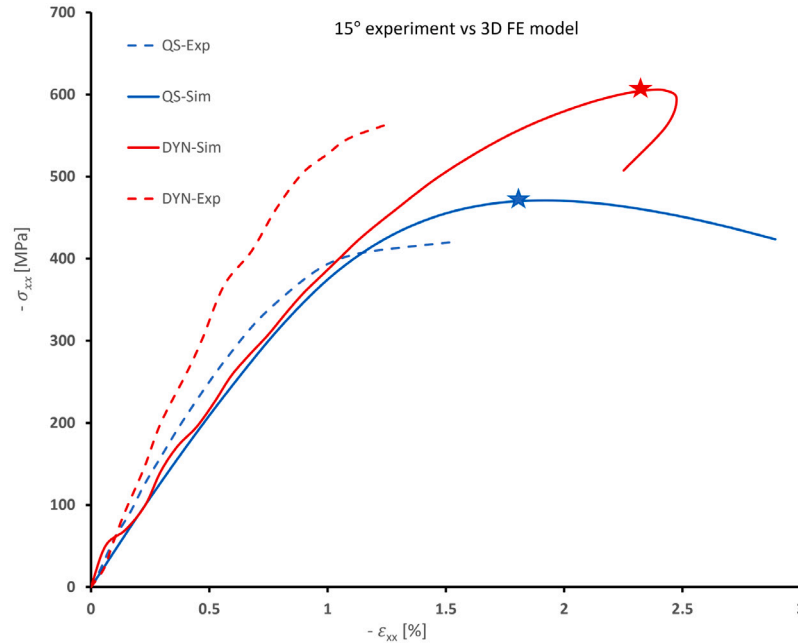
(a) stress-strain response computed based on reaction force and average straining in the center of the specimen.

(b) fibre rotation in QS experiment

(c) fibre rotation in QS FE-simulation
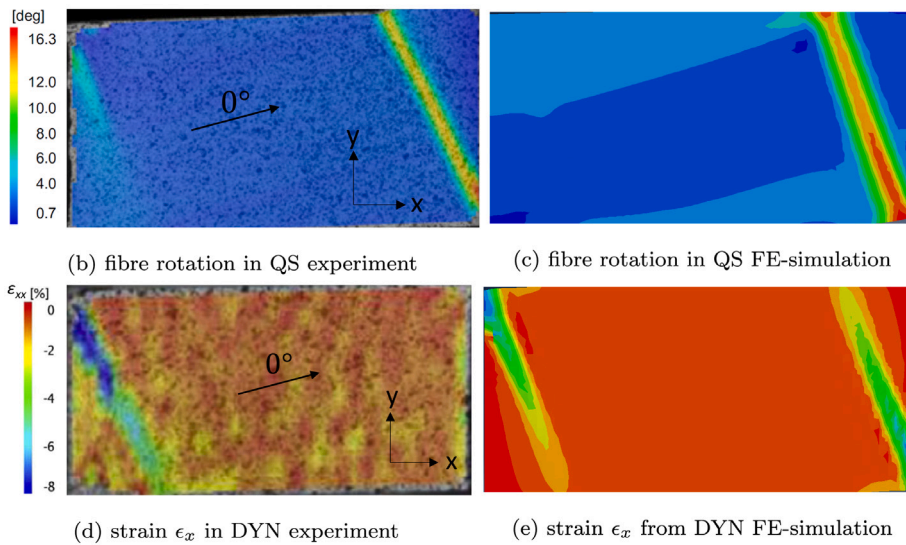
(d) strain ϵ_x in DYN experiment

(e) strain ϵ_x from DYN FE-simulation

Fig. 7. Measured and predicted quasi-static (QS) and dynamic (DYN) failure of 15° off-axis specimen in compression. Experiments are from Koerber et al. (2010). The distribution maps of fibre rotation angle β and axial straining ϵ_x are taken in the vicinity of softening onset, indicated by the markers in 7(a).

evolution law, (Larsson et al., 2018; Razanica et al., 2019). In this paper the damage driving energy covers elastic and plastic work contributions to describe the quasi-brittle compressive failure of the UD-composite. A local damage evolution law is considered to describe the fracture energy release within the diffuse fracture area. An obvious further development is the extension to gradient damage from the developments in Larsson et al. (2018). From the micromechanical coupling between constituents via the isostatic stress condition transverse to the fibres, the matrix damage induce degraded fibre and homogenized responses at the ply level. With respect to the application to crash applications, the model in Larsson et al. (2020) has been placed on the context of general kinematics. This relates to the homogenized stress, where the
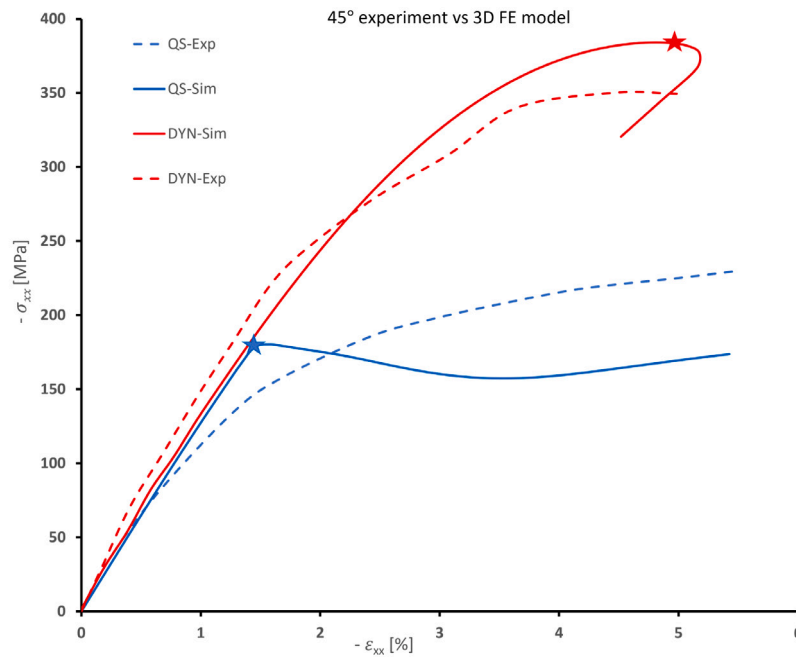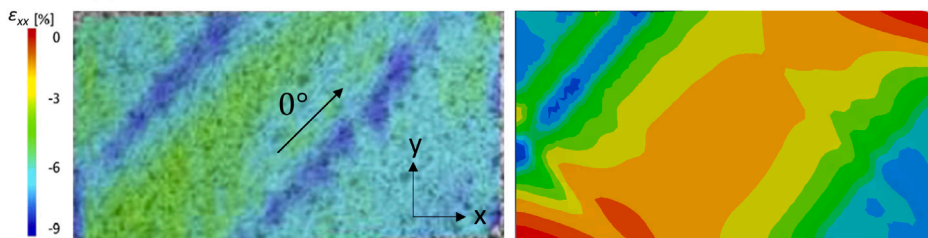
(a) stress-strain response computed based on reaction force and average straining in the center of the specimen.
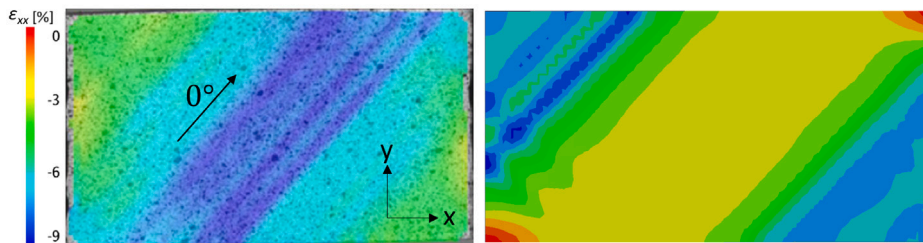
(b) strain ϵ_x in QS experiment

(c) strain ϵ_x from QS FE-simulation

(d) strain ϵ_x in DYN experiment
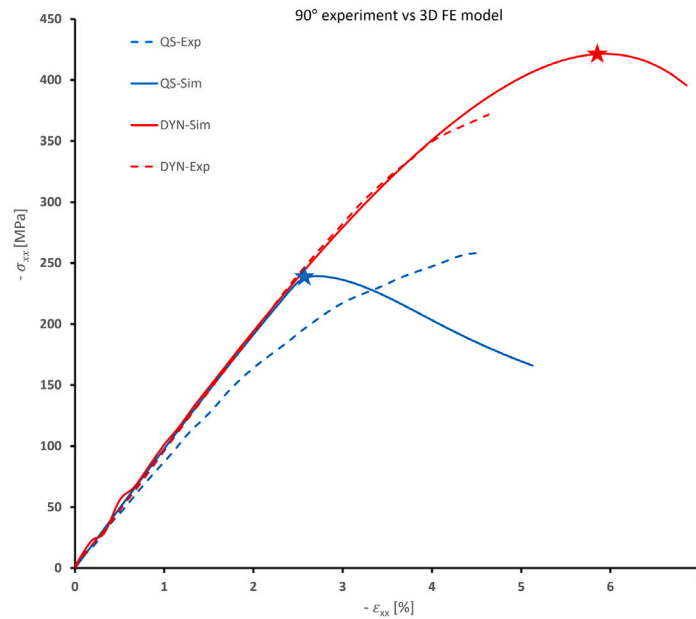

(e) strain ϵ_x from DYN FE-simulation

Fig. 8. Measured and predicted quasi-static (QS) and dynamic (DYN) failure of 45° off-axis specimen in compression. Experiments are from Koerber et al. (2010). The distribution maps of the axial straining are taken in the vicinity of softening onset, indicated by the markers in 8(a).
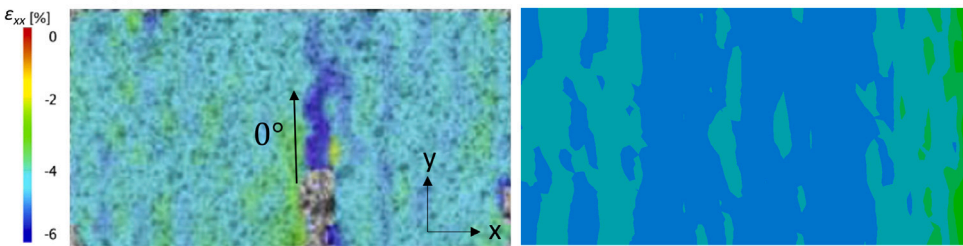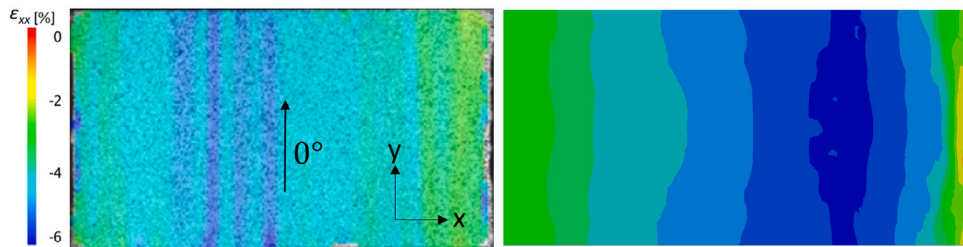
microlevel strain field is described in the Lagrange strain, as well as the inelastic matrix and transverse elastic fibre responses.

An off-axis loaded specimen from the experiment in Koerber et al. (2010) is considered to validate the model behaviour. The model was compared to experimental results of a IM7/8552 UD polymer composite in quasi-static and dynamic compression loading. Relatively good qualitative and quantitative correlations were achieved between the numerical models and experimental results under dynamic loading. The model response clearly reflects the strain rate dependencies and softening due to the progressive damage response under compressive loadings focused in this paper. As expected, observed stress–strain curves under quasi-static and dynamic loading exhibit a nonlinear

quasi-brittle behaviour of the composite in compression. Compared to the more localized strains in the dynamic cases, the strain distributions are generally more diffuse in the quasi-static loading cases. The different failure mechanisms of composite materials under various strain rates are also in-line with other relevant studies (Sassi et al., 2019; Kim et al., 2019; Fan and Wang, 2018). A limiting (and simplifying) assumption is the piecewise constant strain field for the constituents. In this way we do not exactly describe the microstructure of the composite and the consequent microscopic strain field, which influences the homogenized response. This effect is less visible in the dynamic case, where the response is dominated by the viscous effects from calibrated viscous parameters, but becomes apparent in the

(a) stress-strain response computed based on reaction force and average straining in the center of the specimen.

(b) strain ϵ_x in QS experiment

(c) strain ϵ_x from QS FE-simulation

(d) strain ϵ_x in DYN experiment

(e) strain ϵ_x from DYN FE-simulation
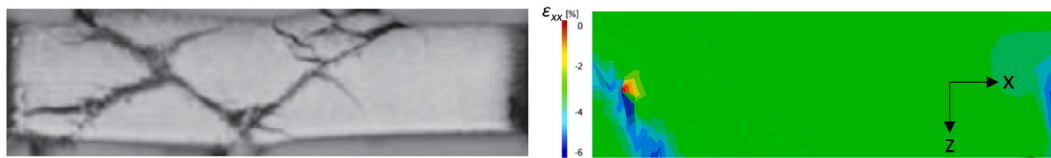
(f) Crack growth in DYN experiment (out-of-plane)

(g) Crack growth in DYN FE-simulation (out-of-plane)

Fig. 9. Measured and predicted quasi-static (QS) and dynamic (DYN) failure of 90° off-axis specimen in compression. Experiments are from Koerber et al. (2010). The distribution maps of the axial straining are taken in the vicinity of softening onset, indicated by the markers in 9(a).

quasi-static case, where viscous effects are absent. On the other hand, a relatively simple micromechanically motivated prototype model is achieved, which we intend use for crash analyses of large scale structural composites. Clearly, the simplicity of the homogenized model contributes to reduced computational cost.

Declaration of competing interest

The authors declare that they have no known competing financial interests or personal relationships that could have appeared to influence the work reported in this paper.

Acknowledgement

References

Ambati, M., Gerasimov, T., De Lorenzis, L., 2015. A review on phase-field models of brittle fracture and a new fast hybrid formulation. Comput. Mech. 55, 383–405.

Camanho, P., Bessa, M., Catalanotti, G., Vogler, M., Rolfes, R., 2013. Modeling the inelastic deformation and fracture of polymer composites – Part II: Smeared crack model. Mech. Mater. 59 (doi: 10.1016/j.mechmat.2012.12.001), 36–49.

Costa, S., Gutkin, R., Olsson, R., 2017. Mesh objective implementation of a fibre kinking model for damage growth with friction. Compos. Struct. 168, 384–391.

Dasappa, P., Lee-Sullivan, P., Xiao, X., 2009. Temperature effects on creep behavior of continuous fiber GMT composites. Composites A 40 (8), 1071–1081.

Eskandaria, S., Pires, F., Camanho, P., Cuic, H., Petrinica, N, Marques, A., 2019. Analyzing the failure and damage of FRP composite laminates under high strain rates considering visco-plasticity. Eng. Fail. Anal. 101 (doi: 10.1016/j.engfailanal.2019.03.008), 257–273.

Fan, J., Wang, C., 2018. Dynamic compressive response of a developed polymer composite at different strain rates. Composites B 152, 96–101.

Gerbaud, P.-W., Otero, F., Bussetta, P., Camanho, P.P., 2019. An invariant based transversely-isotropic constitutive model for unidirectional fibre reinforced composites considering the matrix viscous effects. Mech. Mater. 138 (doi: 10.1016/j.mechmat.2019.103146).

Gutkin, R., Costa, S., Olsson, R., 2016. A physically based model for kink-band growth and longitudinal crushing of composites under 3D stress states accounting for friction. Compos. Sci. Technol. 135, 39–45.

Hexcel Corporation. Stamford, C.T., 2020a. Hexply 8552 product data sheet. EU version. URL https://www.hexcel.com/Site/Resources/DataSheets/Prepreg.aspx.

Hexcel Corporation. Stamford, C.T., 2020b. HexTow IM7 carbon fibre datasheet. Global version. URL https://www.hexcel.com/Resources/DataSheets/Carbon-Fiber.

Kaliske, M., 2000. A formulation of elasticity and viscoelasticity for fibre reinforced material at small and finite strains. Comput. Methods Appl. Mech. Engrg. 185, 225–243.

Kim, D.H., Kang, S.Y., Kim, H.J., Kim, H.S., 2019. Strain rate dependent mechanical behavior of glass fiber reinforced polypropylene composites and its effect on the performance of automotive bumper beam structure. Composites B 166, 483–496.

Koerber, H., Kuhn, P., Ploeckl, M., Otero, F., Gerbaud, P.-W., Rolfes, R., Camanho, P., 2018. Experimental characterization and constitutive modeling of the non-linear stress–strain behavior of unidirectional carbon–epoxy under high strain rate loading. Adv. Model. Simul. 5:17, http://dx.doi.org/10.1186/s40323-018-0111-x.

Koerber, H., Xavier, J., Camanho, P., 2010. High strain rate characterisation of unidirectional carbon-epoxy IM7/8552 in transverse compression and in-plane shear using digital image correlation. Mech. Mater. 42 (11), 1004–1019.

Ladeveze, P., LeDantec, E., 1992. Damage modeling of the elementary ply for laminated composites. Compos. Sci. Technol. 43, 257–267.

Larsson, R., Gutkin, R., Rouhi, S.M., 2018. Damage growth and strain localization in compressive loaded fiber reinforced composites. Mech. Mater. 127, 77–90.

Larsson, R., Razanica, S., Josefson, B.L., 2015. Mesh objective continuum damage models for ductile fracture. Internat. J. Numer. Methods Engrg. 106, 840–860.

Larsson, R., Singh, V., Olsson, R., Marklund, E., 2020. A micromechanically based model for strain rate effects in unidirectional composites. Mech. Mater. 148 (103491), 193–212.

Lemaitre, J., 1992. A Short Course in Damage Mechanics. Springer-Verlag.

Ljustina, G., Fagerström, M., Larsson, R., 2012. Hypo and hyperelasticity applied to modeling of compacted graphite iron machining simulations. Eur. J. Mech. A Solids 374, 57–68.

Maimí, P., Camanho, P.P., Mayugo, J.A., Dávila, C.G., 2007. A continuum damage model for composite laminates: Part I – constitutive model. Mech. Mater. 39 (10), 897–908.

Mamalis, A.G., Robinson, M., Manolakos, D.E., Demosthenous, G.A., Ioannidis, M.B., Carruther, J., 1997. Crashworthy capability of composite material structures. Compos. Struct. 37, 109–134.

Marklund, E., Eitzenberger, J., Varna, J., 2008. Nonlinear viscoelastic viscoplastic material model including stiffness degradation for hemp/lignin composites. Compos. Sci. Technol. 68 (9), 2156–2162.

Melro, A.R., Camanho, P.P., Andrade Pires, F.M., Pinho, S.T., 2013. Micromechanical analysis of polymer composites reinforced by unidirectional fibres: Part I – constitutive modelling. Int. J. Solids Struct. 50, 1897–1905.

Miehe, C., 2011. A multi-field incremental variational framework for gradient-extended standard dissipative solids. J. Mech. Phys. Solids 59, 898–923.

Miehe, C., Hofacker, M., Welschinger, F., 2010a. A phase field model for rate-independent crack propagation: Robust algorithmic implementation based on operator splits. Comput. Methods Appl. Mech. Engrg. 199, 2765–2778.

Miehe, C., Welschinger, F., Hofacker, M., 2010b. Thermodynamically consistent phase-field models of fracture: Variational principles and multi-field FE implementations. Internat. J. Numer. Methods Engrg. 83, 1273–1311.

Peerlings, R.H.J., de Borst, R., Brekelmans, W.A.M., de Wree, J.H.P, 1996. Gradient enhanced damage for quasi-brittle materials. Internat. J. Numer. Methods Engrg. 39 (19), 3391–3403.

Pupure, S., Varna, J., Basso, M., 2018. Effect of degree of cure on viscoplastic shear strain development in layers of [45/-45]s glass fibre/ epoxy resin composites. J. Compos. Mater. 52 (24), 3277–3288.

Razanica, S., Larsson, R., Josefson, B.L., 2019. A ductile fracture model based on continuum thermodynamics and damage. Mech. Mater. 139 (103197).

Sassi, S., Tarfaoui, M., Ben Yahia, H., 2019. Strain rate effects on the dynamic compressive response and the failure behavior of polyester matrix. Composites B 174, 107040.

Sierakowski, R.L., 1997. Strain rate effects in composites. Appl. Mech. Rev. 50 (12), 741–761.

Singh, V., 2018. Literature survey of strain rate effects on composites. Swerea (now RISE) SICOMP, Mölndal, Sweden. TR18-001 (open).

Tan, W., Liu, B., 2020. A physically-based constitutive model for the shear-dominated response and strain rate effect of carbon fibre reinforced composites. Composites B 193 (doi: 10.1016/j.compositesb.2020.108032).

Zhu, G., Sun, G., Yu, H., Li, S., Li, Q., 2018. Energy absorption of metal, composite and metal/composite hybrid structures under oblique crushing loading. Int. J. Mech. Sci. 135, 458–483.